Spatial distribution of turbulent mixing in the upper ocean of the South China Sea

Xiao-Dong Shang[1], Chang-Rong Liang[1,2], and Gui-Ying Chen[1]

[1]State Key Laboratory of Tropical Oceanography, South China Sea Institute of Oceanology, Chinese Academy of Sciences, Guangzhou 510301, China

[2]University of Chinese Academy of Sciences, Beijing 100049, China

Correspondence to: Xiao-Dong Shang (xdshang@scsio.ac.cn)

Abstract. The spatial distribution of the dissipation rate (ε) and diapycnal diffusivity (κ) in the upper ocean of the South China Sea (SCS) is presented from a measurement program conducted from 26 April to 23 May 2010. In the vertical distribution, the dissipation rates were predominantly high in the thermocline where the shear and stratification were strong. In the regional distribution, high dissipation rate and diapycnal diffusivity were observed in west of the Luzon Strait with an average dissipation rate and diapycnal diffusivity of 8.3×10^{-9} W kg^{-1} and 2.7×10^{-5} m^2 s^{-1}, respectively, almost one order of magnitude higher than those in the central and southern SCS. In west of the Luzon Strait, the water column was characterized by strong shear and weak stratification. Elevated dissipation rates ($\varepsilon > 10^{-7}$ W kg^{-1}) and diapycnal diffusivity ($\kappa > 10^{-4}$ m^2 s^{-1}) induced by shear instability occurred in the water column. In the central and southern SCS, the water column was characterized by strong stratification and weak shear and the turbulent mixing was weak. The observed dissipation rates were found to scale positively with the shear and stratification, which was consistent with the MacKinnon-Gregg model used for the continental shelf, but different from the Gregg-Henyey scaling used for the open ocean.

1 Introduction

Turbulent mixing is a crucial mechanism that controls the distribution of nutrients, sediments, fresh water, and pollutants throughout the water column [Sandstrom and Elliott, 1984]. The magnitude and distribution of diapycnal diffusivity are important for large-scale ocean circulation [Saenko and Merryfield, 2005]. Assuming a balance between vertical advection and vertical diffusion for tracers, Munk [1966] reported that a global average diapycnal diffusivity of 10^{-4} m s^{-1} is required to maintain gross oceanic stratification and overturning circulation. However, measurements of ocean turbulence and released tracers [Ledwell et al., 1993] have implied the diapycnal diffusivity in the ocean interior of only 10^{-5} m^2 s^{-1}, which is one-tenth of the value predicted by most ocean circulation models. Therefore, it has been argued that elevated mixing concentrated in rough topographies [Ledwell et al., 2000; Wu et al., 2011] would aid in explaining this discrepancy. In the past decade, elevated diapycnal diffusivities, i.e., O $(10^{-4}$ m^2 s$^{-1})$ or higher, have been found in mixing hotspots such as seamounts [Carter et al., 2006; Lueck and Mudge, 1997], ridges [Klymak et al., 2006; Lee et al., 2006], and canyons [Carter and Gregg, 2002]. However, these elevated mixing events are highly localized. Whether such

topographically enhanced mixing is sufficiently intense or widespread to significantly increase the basin-wide average remains unclear. Using a simple averaging scheme, Kunze and Toole [1997] suggested that topographically induced mixing was insufficient to support a basin-averaged diffusivity of O (10^{-4} m^2 s^{-1}) above a 3000 m depth in the North Pacific.

Compared with the open ocean, less attention has been given to marginal seas. In recent years, observations [Tian et al., 2009] indicated that turbulent mixing in marginal seas could make an important contribution to ocean mixing. The South China Sea (SCS), one of the largest marginal seas of the Pacific, connects to the Pacific through the Luzon Strait. Measurements and numerical simulations [Alford et al., 2015; Chang et al., 2006; Lien et al., 2005] indicated that large numbers of energetic internal tides and internal waves generated near the Luzon Strait propagate into the SCS and facilitate turbulent mixing. Considerable effort has been put forth to explore the characteristics of turbulent mixing in the SCS. Using fine-scale parameterization, Tian et al. [2009] reported a turbulent mixing distribution along a section from the northern SCS to Pacific and found that the diapycnal diffusivity in the upper 500 m of the northern SCS reached O (10^{-5} m^2 s^{-1}), almost two orders larger than that in the Pacific. With the Gregg-Henyey-Polzin parameterization, Yang et al. [2016] presented a three-dimensional distribution of turbulent mixing in the SCS and found diapycnal diffusivity of O (10^{-2} m^2 s^{-1}) in the bottom water of the Luzon Strait and the Zhongsha Island Chain area. In addition to these parameterizations, some direct measurements from microstructure profilers are also available. A direct observation of turbulent dissipation was reported by Laurent [2008] who found dissipation rate as high as 10^{-6} W kg^{-1} in the shelf break of the northern SCS. Lozovatsky et al. [2013] reported regional mapping of the averaged dissipation rate in the upper pycnocline of the northern SCS and found values in the Luzon Strait as high as 10^{-7} W kg^{-1}. Yang et al. [2014] conducted direct measurements of turbulence along a section across the continental shelf and slope in the northern SCS. Their results show that the averaged dissipation rate over the shelf reached 10^{-7} W kg^{-1}, which is an order of magnitude larger than that over the slope. There is no doubt that these studies have greatly aided our knowledge of turbulent mixing in the SCS. However, the direct microstructure measurements are localized and scattered with most of them focusing on the northern SCS. Few microstructure measurements have been conducted in the central and southern SCS. In addition, there is a lack of studies assessing the parameterizations in the SCS, though they are important to the ocean models. In this work, we present a more complete direct microstructure measurement in the upper ocean of the SCS and explore the associated mixing regimes. Two fine-scale parameterizations are tested against microstructure measurements, which provide useful reference for modelers.

2 Measurements and Methods

The field experiment was performed prior to the South China Sea summer monsoon (SCSSM) onset from LT 26 April to 23 May 2010. A total of 82 stations were conducted in the experiment (Fig. 1). Direct turbulence measurements were collected with the Turbulence Ocean Microstructure Acquisition Profiler (TurboMAP), which is a loosely tethered, free-falling instrument ballasted to fall at 0.5-0.7 m s^{-1} and measure the microstructure of the velocity shear u_z. The TurboMAP profiler is also equipped with other sensors for measuring in situ temperature, pressure, conductivity, chlorophyll, and

turbidity variations [Wolk et al., 2002]. The sampling frequency is 512 Hz and the measurement depth range is limited to

800 m. Approximately 30 min elapsed at shallow stations or 1 h in deep water for each down- and up-cast. Continuous time

65   series of velocity at 5-min intervals and 16-m vertical spacing between 38 and 982 m were obtained from a shipboard ADCP.

The CTD casts were conducted to provide measurements of temperature and salinity. Data obtained from six moorings (Fig.

1, yellow squares) were used to perform a brief analysis of the wave field in the SCS. Moorings 1-3 were deployed over the

continental shelf/slope and moorings 4-6 were deployed in the deep basin. More information regarding the moorings is given

in Table 1.

70
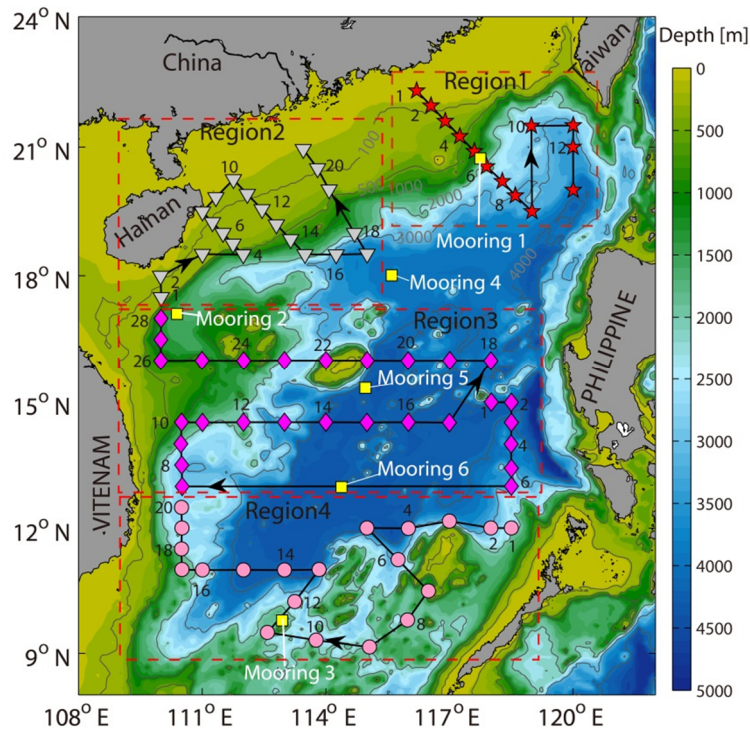
Fig. 1. Bottom topography of the SCS and observation stations (symbols). Red stars indicate the stations located in west of

the Luzon Strait (region 1). Gray triangles indicate the stations located in northeast of Hainan Island (region 2). Magenta

diamonds indicate the stations located in the central SCS (region 3). Pink dots indicate the stations located in the southern

SCS (region 4). Station numbers (i.e., 1, 2, 4…) are indicated in each region. The arrows indicate the order of the

75   measurement. The yellow squares indicate the locations of the moorings.

The dissipation rate is estimated with the micro-shear u_z: $\varepsilon = 7.5\nu\langle u_z^2\rangle = 7.5\nu\int_{k_1}^{k_2}\psi(k)\,dk$, where ν is the kinematic

viscosity, $<>$ denotes the spatial average, $\psi(k)$ is the shear spectra, and k_1 and k_2 are the integration limits. k_1 is set to 1

cpm, and k_2 is the highest wavenumber that is not contaminated by vibration noise. Estimates of ε are computed from the

shear signal with 2-m depth segments based on a spectral analysis of the shear signal from the two probes. Dissipation data

80 are unreliable in the top 11 m due to contamination by the strong tilting of the TurboMAP profiler and ship's wake. Examples of the shear spectra and corresponding estimates of the dissipation rate are given in Fig. 2. The spectra follow the slope of Nasmyth's universal spectrum [Nasmyth, 1970]. Distinct peaks associated with high wave numbers (beyond the upper integration bound) were caused by instrument vibrations. Diapycnal diffusivity $\kappa = \Gamma \varepsilon / N^2$ [Osborn, 1980] was calculated based on the dissipation rate ε, stratification N, and mixing efficiency $\Gamma = 0.2$ [Oakey, 1982]. The shear variance,

85 $S^2 = (\Delta \overline{U} / \Delta z)^2 + (\Delta \overline{V} / \Delta z)^2$, was calculated with $\Delta z = 16$ m, where $\overline{U}$ and $\overline{V}$ are the zonal and meridional components of the mean horizontal velocity, respectively. The mean velocity is averaged over the time intervals of the TurboMAP measurements.
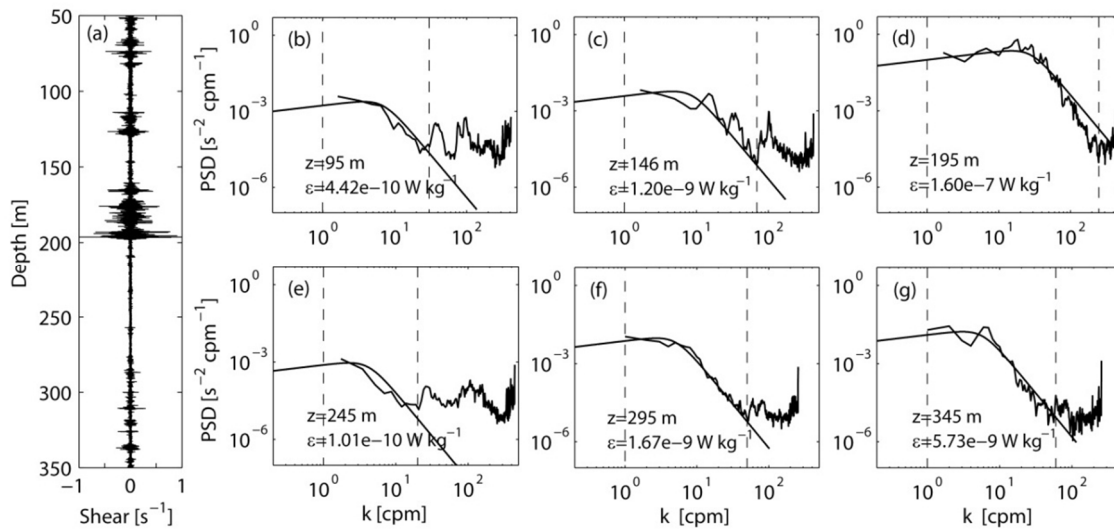
Fig. 2. Examples of (a) micro-shear and (b-g) shear spectra at different depths. The integration bounds (vertical dashed lines)
90 and Nasmyth spectra (smooth curves) are shown.

Table 1. Information about the moorings.

Mooring	Latitude (˚N)	Longitude (˚E)	Water Depth (m)	Measurement Depth Range (m)	Measurement Duration (d/m/yr)	Time Interval (min)	Bin Size (m)
Mooring 1	20.74	117.75	1260	13~454	01/08/14~27/09/14	2	16
Mooring 2	17.10	110.39	1410	6~478	04/05/09~04/09/10	60	8
Mooring 3	9.79	112.74	1680	40~416	25/05/09~10/11/10	60	8
Mooring 4	18.01	115.60	3790	60~370	09/04/98~05/10//98	60	10
Mooring 5	15.34	114.96	4265	30~270	07/10/98~11/04//99	60	10
Mooring 6	12.98	114.38	4370	30~270	09/10/98~12/04//99	60	10

3 Results

3.1 Water mass properties

95   Intrusion of water from the Pacific can influence the evolving water properties in the SCS. It has been confirmed by in situ measurements and models [Shaw, 1991; Wu and Hsin, 2012] that there is a strong intrusion of water from the Pacific into the SCS through the Luzon Strait. Two well-defined water masses are active in this process [Qu et al., 2000]: high-salinity North Pacific Tropical Water (NPTW) and low-salinity North Pacific Intermediate Water (NPIW). For simplicity, we divide the observations into four regions (Fig. 1): region 1 is located in west of the Luzon Strait, region 2 is located in

100   northeast of Hainan Island, region 3 is located in the central SCS, and region 4 is located in the southern SCS. Fig. 3 shows the T-S curves of the SCS and western Pacific. Temperature and salinity data in the western Pacific (18.5^o N-22.5^o N, 124.5^o E-128.5^o E) were obtained from the World Ocean Database 2013 (http://www.nodc.noaa.gov/OC5/woa13/woa13data.html). The T-S curve in the western Pacific shows a reversed 'S' shape with NPTW and NPIW clearly identified (Fig. 3, black dashed curve). NPTW and NPIW correspond to the maximum salinity layer at $\sigma_\theta \in$ (22.5-25.5) kg m^{-3} and minimum salinity

105   layer at $\sigma_\theta \in$ (25.5-27.5) kg m^{-3}, respectively. In the maximum salinity layer (22.5-25.5 kg m^{-3}), the water column in west of the Luzon Strait (region 1) had a salinity maximum of 34.8 psu that approaches the maximum value of the NPTW. Salinity decreased gradually from the Luzon Strait to the Hainan Island (region 2) and to the central and southern SCS (region 3 and region 4). This trend is reversed in the minimum salinity layer (25.5-27.5 kg m^{-3}), where the salinity slightly increased from the Luzon Strait to Hainan Island and to the central and southern SCS. The salinity minimum in the Pacific was found to be

110   lower than that in the SCS. The reverse S shape becomes remarkably weak from the northern SCS to the southern SCS, a change to which turbulent mixing occurring in the SCS might have made a significant contribution.
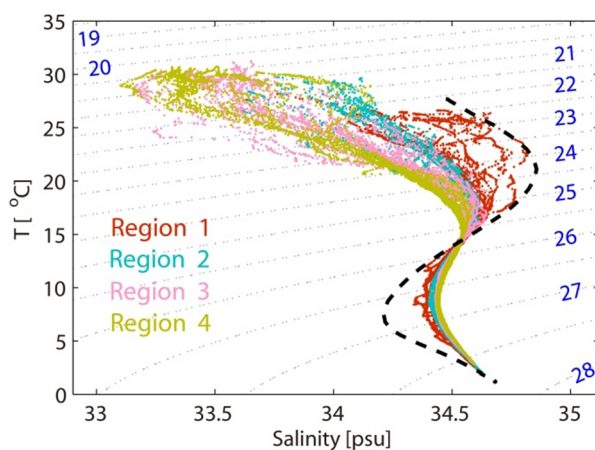
Fig. 3. Relation of potential temperature vs. salinity (with the potential density σ_θ in kg/m^3 contours overlaid) of all stations. The black dashed curve shows the relation for potential temperature vs. salinity of the western Pacific for reference.
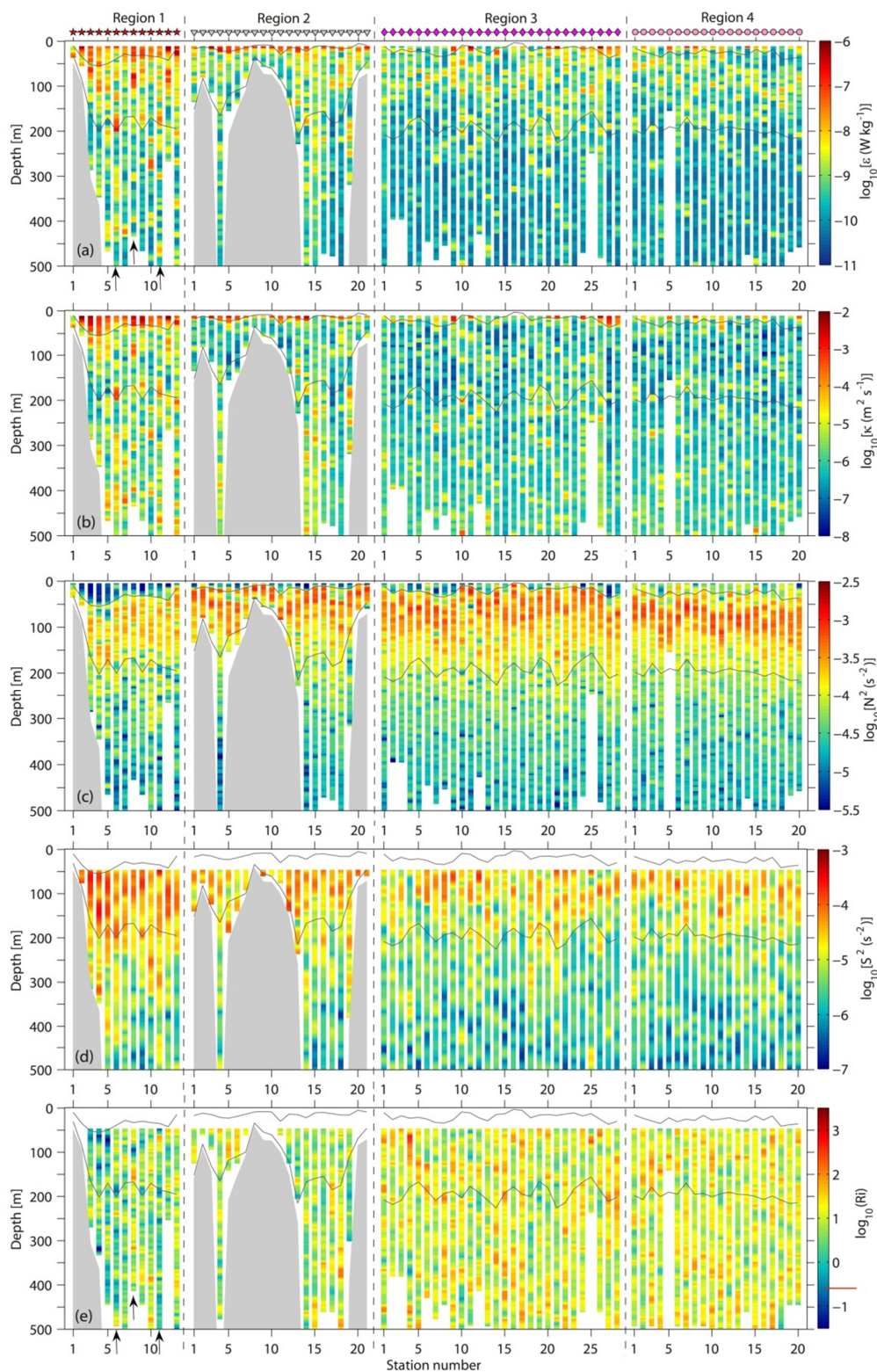
Fig. 4. (a) Dissipation rate (ε), (b) diapycnal diffusivity (κ), (c) buoyancy frequency (N^2), (d) shear variance (S^2), and (e) Richardson number (Ri) from all of the stations. The gray shading indicates the bathymetry. In (a)-(e) the boundaries of the thermocline are indicated (gray curves). The red line on the color bar of (e) represents Ri =0.25. The vertical dashed lines divide the stations into four regions with the symbols (red stars, gray triangles, magenta diamonds, and pink dots) shown at the top of (a). These symbols correspond to the station symbols in Fig. 1.

3.2 Microstructure Measurements

Figure 4a shows the distribution of the dissipation rate with the thermocline boundaries overlain. Different criteria have been used to define the surface mixed layer in terms of either temperature or density. Here, we defined the surface mixed layer as the depth at which the potential temperature change from the surface temperature is 0.5 ˚C. The bottom of the thermocline is defined as the depth at which the temperature gradient is equal to 0.05 ˚C m^{-1}. The surface mixed layers are slightly deep in region 1 compared with the other regions. The average depths of the surface mixed layer in regions 1-4 are 35.2, 14.7, 19.4, and 26.8 m, respectively.

In the surface mixed layer, strong turbulence was accompanied by high dissipation rates (Fig. 4a), which may be attributed to various factors, such as wind stirring, buoyancy flux, and surface waves. Below the surface mixed layer, high dissipation rates (Fig. 4a) were observed in the thermocline, with the average ε in the thermocline reaching 4.6×10^{-9} W kg^{-1}, which was five times larger than the value of 8.2×10^{-10} W kg^{-1} below the thermocline. Strong shear (Fig. 4d) also occurred in the thermocline with an averaged S^2 in the thermocline of 3.3×10^{-5} s^{-2}, which was five times larger than that below the thermocline (6.5×10^{-6} s^{-2}). The strong spatial correlation between dissipation and shear implies that shear played an important role in driving the dissipation. Contrary to the dissipation rate, the diapycnal diffusivity (Fig. 4b) in the thermocline was slightly weaker than that below the thermocline. The high diapycnal diffusivity below the thermocline was mainly due to the relatively weak stratification (Fig. 4c). The average N^2 below the thermocline was 8.4×10^{-5} s^{-2}, four times smaller than the value of 3.4×10^{-4} s^{-2} in the thermocline.

Turbulent mixing in region 1 displayed a different feature from that of the other regions. In region 1, turbulence was more active than in other regions, with the maximum dissipation rate reaching 10^{-6} W kg^{-1} (Fig. 4a) and the maximum diapycnal diffusivity over 10^{-3} m^2 s^{-1} (Fig. 4b). In addition, region 1 had weak stratification but strong shear compared with other regions (Figs. 4c and 4d). Most of the water column in region 1 was occupied by Richardson number ($Ri = N^2/S^2$) of order 1, almost two orders smaller than that in the other regions (Fig. 4e). A distinguishing feature in region 1 is that some turbulent patches with elevated dissipation rates ($\varepsilon >10^{-7}$ W kg^{-1}) and diapycnal diffusivity ($\kappa >10^{-4}$ m^2 s^{-1}) were observed in the water column. These turbulent patches often occurred at depths where the Richardson number was below 0.25; for example, station 6 (between 175 and 195 m), station 8 (between 80 and 100 m), and station 11 (between 175 and 195 m) (indicated by the arrows in Fig. 4), which suggests that elevated dissipation rates and diapycnal diffusivity in the turbulent patches are likely to result from shear instability. More detail regarding the shear instability will be discussed in the following text. Compared with region 1, turbulent mixing in regions 2-4 was relatively weak, with an average ε and κ in the

upper 500 m (not including the surface mixed layer) of 1.1×10^{-9} W kg^{-1} and 3.7×10^{-6} m^2 s^{-1}, respectively. These two values

150 are almost one order of magnitude smaller than those ($\varepsilon \sim 8.3 \times 10^{-9}$ W kg^{-1} and $\kappa \sim 2.7 \times 10^{-5}$ m^2 s^{-1}) in region 1. Weak turbulent mixing in regions 2-4 is likely to be associated with the strong stratification and weak shear. N^2 (Fig. 4c) was greater than S^2 (Fig. 4d) in regions 2-4 with most of the water column occupied by large Richardson number ($Ri>10$) (Fig. 4e).
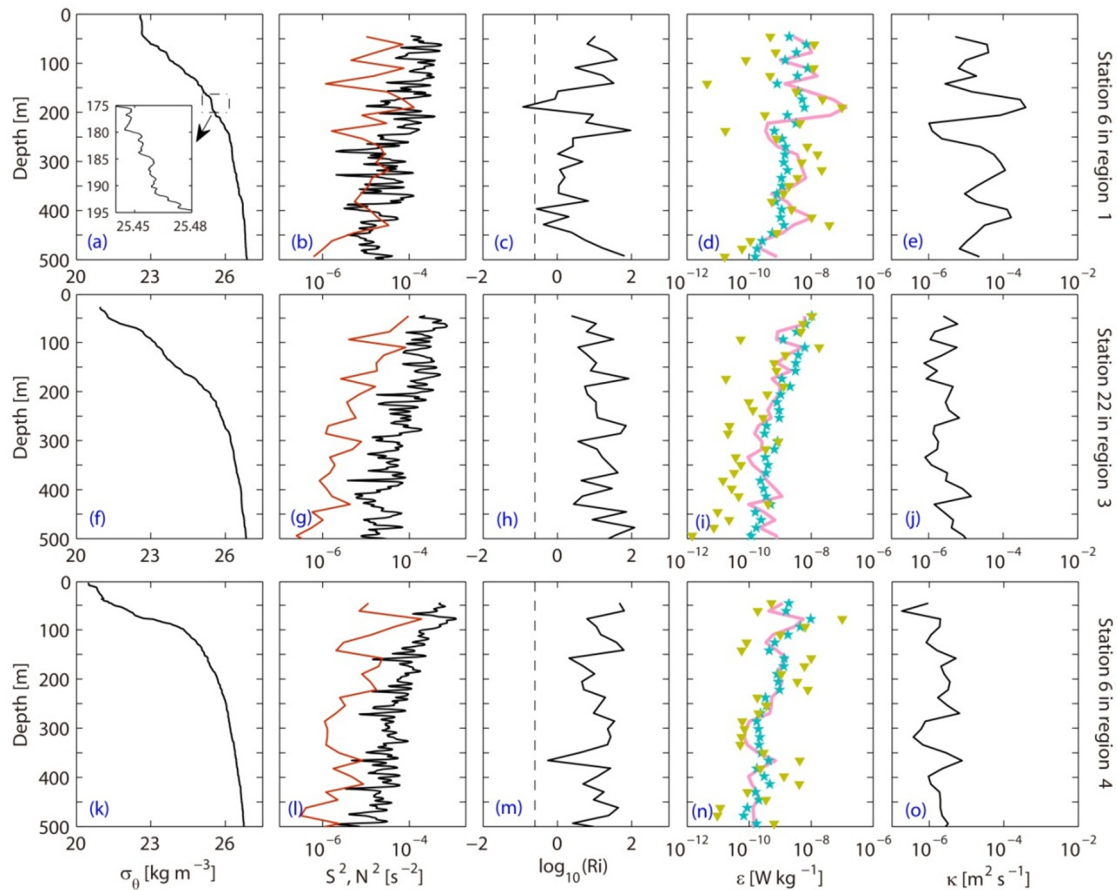
155 Fig. 5. From top to bottom, three sets of profiles are from station 6 in region 1 (top panels), station 22 in region 3 (middle panels), and station 6 in region 4 (bottom panels). For each station, quantities plotted are (from left to right) potential density, shear variance (red) and buoyancy frequency (black), Richardson number (the vertical line indicates $Ri=0.25$), observed (pink curves) MG model (stars) and GH model (triangles) dissipation rates, and observed diapycnal diffusivity. The observed dissipation rate and diapycnal diffusivity have been vertically averaged over the 16 m ADCP bins. The inset in (a) enlarges

160 the density profile to show the overturns.

To further understand the changing pattern of turbulence in the SCS, we now look in detail at the profiles of various quantities at three stations in different regions: station 6 from west of the Luzon strait (region 1), station 22 from the central

SCS (region 3), and station 6 from the southern SCS (region 4). At station 6 in region 1 (Figs. 5a-5e), the shear variance was slightly smaller than the buoyancy frequency over most of the water column (Fig. 5b). However, the shear variance exceeded
165 the buoyancy frequency at some depths; for example, the shear variance was greater than the buoyancy frequency at a depth of 185 m, pushing the Richardson number below 0.25, which implies shear instability (Fig. 5c). Small overturns were also found in the density profile at depths of 175 to 195 m (Fig. 5a, the inset); for example, the potential density at 179.2 m was lower than that at 175.5 m. The dissipation rate (Fig. 5d) and diapycnal diffusivity (Fig. 5e) in the corresponding depths (175-195 m) were elevated by more than one order of magnitude with the diapycnal diffusivity reaching 5.0×10^{-4} m^2 s^{-1}, two
170 orders of magnitude higher than the open-ocean background values of 5.0×10^{-6} m^2 s^{-1} [Gregg, 1989]. The dissipation rates induced by shear instability contributed significantly to the turbulent mixing in the water column. Nearly 45% of the total dissipation rate in the upper 500 m (not including the surface mixed layer) was contributed by the elevated dissipation rate from the turbulent patch. The second and third sets of profiles were from region 3 (Figs. 5f-5j) and region 4 (Figs. 5k-5o), respectively. The buoyancy frequency was higher than the shear variance (Figs. 5g and 5l), and no Richardson numbers
175 below 0.25 were observed (Figs. 5h and 5m). The water column was occupied by dissipation rates ranging from 10^{-10} to 10^{-9} W kg^{-1} (Figs. 5i and 5n) and diapycnal diffusivity of O (10^{-6} m^2 s^{-1}) (Figs. 5j and 5o), that is, the same level as the background of the open ocean.

Because the dissipation rates were dominantly large in the thermocline, we calculate the averaged dissipation rate $<\varepsilon>_T$ as well as the averaged diapycnal diffusivity $<\kappa>_T$ in the thermocline to compare the magnitudes of the dissipation rate and
180 diapycnal diffusivity in different regions. $<\varepsilon>_T$ and $<\kappa>_T$ are given by

$$\langle\varepsilon\rangle_T = 1/(z_b - z_t) \int_{z_b}^{z_t} \varepsilon dz \text{ and } \langle\kappa\rangle_T = 1/(z_b - z_t) \int_{z_b}^{z_t} \kappa dz,$$

where z_b and z_t are the bottom and top locations of the thermocline, respectively. The dissipation rate and diapycnal diffusivity affected by the surface mixed layer were excluded before calculating $<\varepsilon>_T$ and $<\kappa>_T$. Fig. 6a shows the averaged dissipation rate in the thermocline. $<\varepsilon>_T$ displayed a decreasing trend toward the south from O (10^{-8} W kg^{-1}) in west of the
185 Luzon Strait (region 1) to O (10^{-9} W kg^{-1}) in the southern SCS (region 4). In region 1, $<\varepsilon>_T$ ranged from 1.8×10^{-9} to 5.0×10^{-8} W kg^{-1} with a mean value of 1.8×10^{-8} W kg^{-1}, which was 7 times, 9 times, and 12 times higher than the mean values of region 2 (2.5×10^{-9} W kg^{-1}), region 3 (2.1×10^{-9} W kg^{-1}), and region 4 (1.5×10^{-9} W kg^{-1}), respectively. Elevated $<\kappa>_T$ was also observed in region 1 (Fig. 6b). The average $<\kappa>_T$ in region 1 was 3.5×10^{-5} m^2 s^{-1}, which was an order of magnitude greater than the values of region 2 (3.3×10^{-6} m^2 s^{-1}), region 3 (2.2×10^{-6} m^2 s^{-1}), and region 4 (2.1×10^{-6} m^2 s^{-1}). One prominent
190 feature in the northern SCS is that the mean of $<\kappa>_T$ in region 1 was 11 times higher than the value in region 2 while the mean of $<\varepsilon>_T$ in region 1 was only 7 times higher than that the value in region 2. This difference mainly resulted from the weak stratification in region 1 (Fig. 4c).

Microstructure measurements at different stations were taken at different times; thus, spring-neap tides may be one of the factors that affect the variability of $<\varepsilon>_T$ and $<\kappa>_T$. To explore the effect of spring-neap tides on the variability of $<\varepsilon>_T$
195 and $<\kappa>_T$, we obtained the barotropic tides from the global inverse tide model (TPXO) [Egbert and Erofeeva, 2002], which

give us the time information of spring-neap tides during the period of observation. Only the barotropic tides at 18°N, 114°E were extracted because the spring-neap tides in different locations of the SCS occur almost simultaneously. The 14-day spring-neap cycles were well-represented in the extracted barotropic tides (Fig. 6c). A comparison of $<\varepsilon>_T$ and $<\kappa>_T$ to the extracted tides suggests that the main variability of $<\varepsilon>_T$ and $<\kappa>_T$ and their distribution characteristics were not attributed to

200   the effect of spring-neap tides; for example, though stations in regions 1 and 3 spanned neap and spring tides (see Fig. 6c, stars and diamonds), the averaged $<\varepsilon>_T$ and $<\kappa>_T$ in region 1 were still an order of magnitude greater than the values in region 3 (Figs. 6a and 6b); furthermore, stations 1-6 in region 3 were conducted during the spring tide (Fig. 6c, 2 May to 3 May, diamonds), but their $<\varepsilon>_T$ and $<\kappa>_T$ values were slightly lower than those of stations 7-17, which were measured during the neap tide (Fig. 6c, 9 May to 12 May, diamonds).
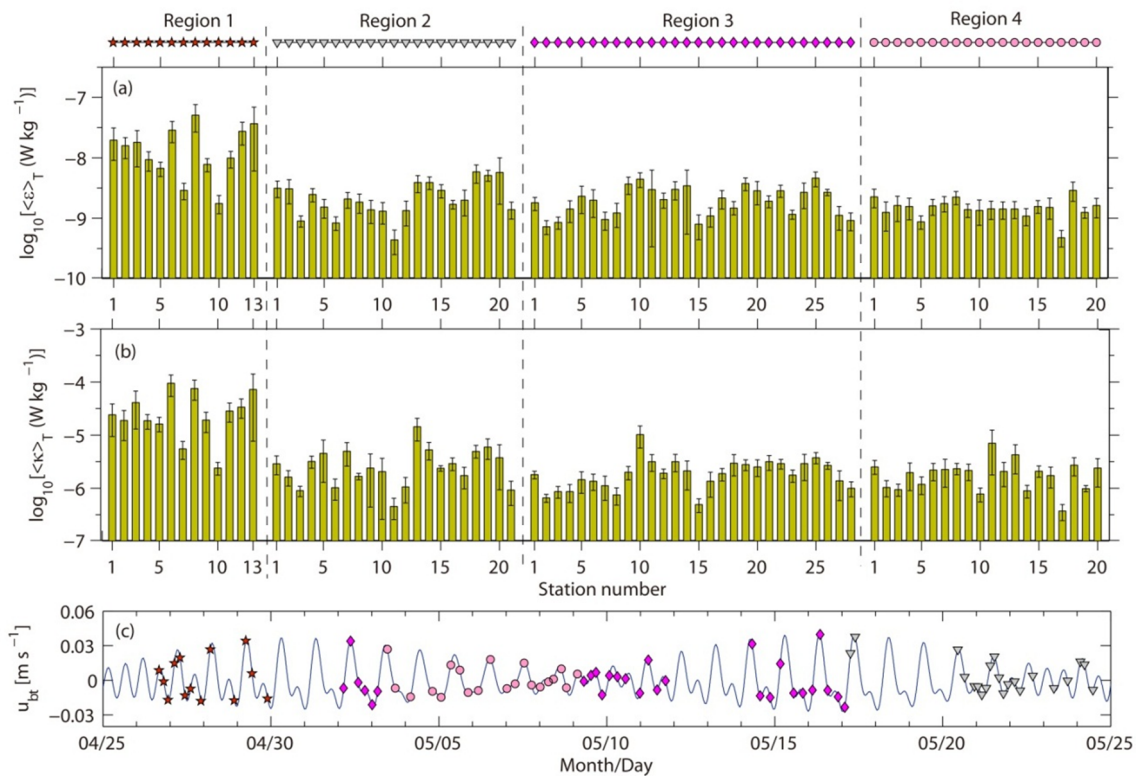
205

Fig. 6. (a) The average dissipation rate $<\varepsilon>_T$ and (b) the average diapycnal diffusivity $<\kappa>_T$ in the thermocline. The vertical lines indicate the 95% bootstrapped confidence interval. The vertical dashed lines divide the stations into four regions with symbols (red stars, gray triangles, magenta diamonds, and pink dots) shown at the top of (a). These symbols correspond to the station symbols in Fig. 1. (c) Time series of the barotropic tidal velocity (u_{bt}) predicted from TPXO 7.1 with the station

210   symbols overlain.

Here we provide a brief summary for this section. Our observation indicates that strong turbulent mixing was concentrated in west of the Luzon Strait (region 1), with stratification and shear variance made significant contributions. The water column in region 1 had weaker stratification but stronger shear than those in other regions. In this condition, shear instability events occasionally occurred in region 1 and produced elevated dissipation and diapycnal diffusivity. In regions 2-

215 4, instead, the water column was characterized by weak shear and strong stratification. Shear was no longer sufficiently high to produce subcritical Richardson numbers. The resulting turbulence was weak. Our analysis indicates that the spatial distribution of turbulent mixing with large $<\varepsilon>_T$ and $<\kappa>_T$ concentrated in west of Luzon Strait does not result from the effect of spring-neap tides.

3.3 Parameterizations of turbulence

220 In this section we evaluate two models for parameterizing the dissipation rate in terms of more easily observed or modeled quantities, such as stratification and shear. One wave-wave interaction parameterization [Gregg, 1989; MacKinnon and Gregg, 2003] in the open ocean is the Gregg-Henyey scaling (known as the GH model) given by

$$\varepsilon_{GH} = 1.8 \times 10^{-6} f \, cosh^{-1}\left(\frac{N_0}{f}\right)\left(\frac{S^4}{S_{GM}^4}\right)\left(\frac{N^2}{N_0^2}\right) \text{ and}$$

$$S_{GM}^4 = 1.66 \times 10^{-10}\left(\frac{N^2}{N_0^2}\right)^2,$$

where f is the Coriolis frequency, S is the low-frequency/low-mode resolved shear, and N_0 is a reference buoyancy frequency. Another analytical model [MacKinnon and Gregg, 2003] is the MacKinnon-Gregg model (known as the MG

225 model) given by

$$\varepsilon_{MG} = \varepsilon_0\left(\frac{N}{N_0}\right)\left(\frac{S}{S_0}\right),$$

where $S_0=N_0=3$ cph and ε_0 is an adjustable constant that gives the model dissipation rate the same cruise average as the observational data. The adjustable constant ε_0 shows great variability in different regions and seasons, spanning from 10^{-10} W kg^{-1} to more than 10^{-8} W kg^{-1} [MacKinnon and Gregg, 2005; Palmer et al., 2008; van der Lee and Umlauf, 2011; Xie et al., 2013]. This regional and temporal variability of ε_0 strongly suggests the importance of different physical processes on setup

230 and maintenance of the background levels of turbulent dissipation. Here, we assess the two models for parameterization of the turbulence in the northern SCS (dissipation data are from the stations in region 1 and region 2), central SCS (dissipation data are from the stations in region 3), and southern SCS (dissipation data are from the stations in region 4). Different values of parameter ε_0 are selected for the parameterizations due to their different mixing backgrounds: $\varepsilon_0=1.65\times10^{-9}$ W kg^{-1} for the northern SCS, $\varepsilon_0=0.96\times10^{-9}$ W kg^{-1} for the central SCS, and $\varepsilon_0= 0.50\times10^{-9}$ W kg^{-1} for the southern SCS. All of the data

235 affected by the surface mixed layers or bottom mixed layers were excluded for the parameterizations. To reduce the bias introduced by the different vertical resolutions of the shear and stratification data, density was first interpolated onto the

ADCP grid and N^2 was computed from finite differencing. Accordingly, the dissipation rates were vertically averaged over the 16-m ADCP bins.

The results of the parameterizations are shown in Fig. 7. The observed dissipation rates in the SCS (Fig. 7, left column)
240 increased with increasing buoyancy frequency and shear. The GH model fails to reproduce these kinematic relationships (Fig. 7, right column). The dependence of ε_{GH} on shear is too strong, with the dissipation rates underestimated in weak shear. ε_{GH} also varies inversely with the buoyancy frequency for a given level of shear, contrary to the observation (Fig. 7, left column). Instead, the MG model dissipation rates (Fig. 7, middle column) display a qualitatively consistent pattern with the observed data (Fig. 7, left column). Both the observed and MG model dissipation rates scale positively with shear and the buoyancy
245 frequency. In the northern SCS, the turbulence was more complicated than the predictions of the MG model. The MG model (Fig. 7b) underestimated the elevated dissipation rates that scattered in Fig. 7a; for example, the MG model underestimated the elevated dissipation rates at (N^2=6.5×10^{-5} s^{-2}, S^2=5.0×10^{-6} s^{-2}), (N^2=1.0×10^{-4} s^{-2}, S^2=1.0×10^{-5} s^{-2}), and (N^2=7.9×10^{-5} s^{-2}, S^2=2.0×10^{-5} s^{-2}).
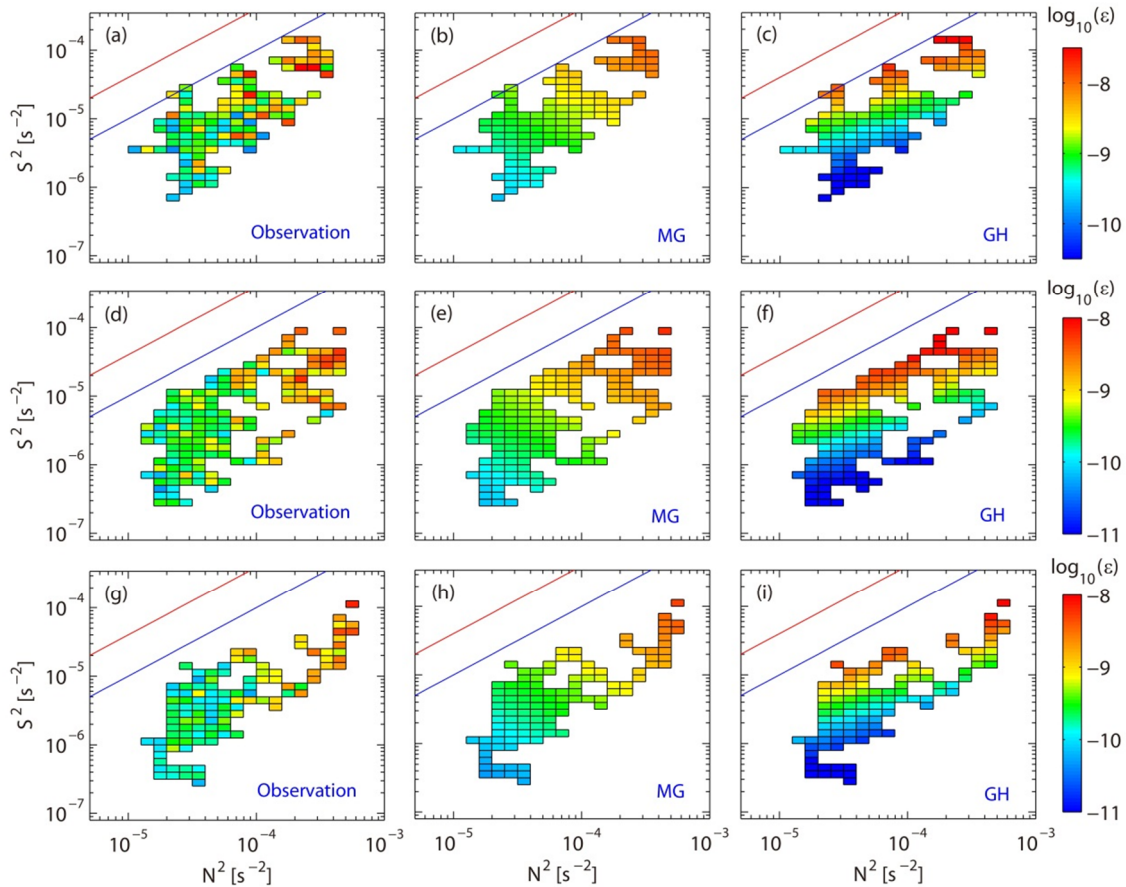
250 Fig. 7. Dissipation rates of observation ε_{OB} (left column), MG model ε_{MG} (middle column), and GH model ε_{GH} (right column) averaged in bins of 16 m buoyancy frequency (N^2) and 16 m shear variance (S^2). All data affected by the surface

mixed layers or bottom mixed layers were excluded. (a-c) show the results of the stations in the northern SCS, (d-f) show the results of the stations in the central SCS, and (g-i) show the results of the stations in the southern SCS. The boundaries of Ri=0.25 (oblique red lines) and Ri=1 (oblique blue lines) are shown for reference.

255   To further evaluate the success of the two models in parameterizing the observed dissipation rates, we explore the separate shear and buoyancy frequency dependence (Fig. 8). They are equivalent to integrating the two-dimensional plots in Fig. 7 horizontally and vertically. Both models reproduce the slope of the dissipation rate versus the buoyancy frequency ($\varepsilon \propto N^2$) (Figs. 8a, 8c, and 8e), though the GH model dissipation rates are too large on average. However, the two models show large differences in the trend of the dissipation rate versus shear (Figs. 8b, 8d, and 8f). The MG model successfully

260   captures the essential kinematic relationship between the dissipation rate and shear, whereas the GH model dissipation rates have a much steeper relationship with shear.
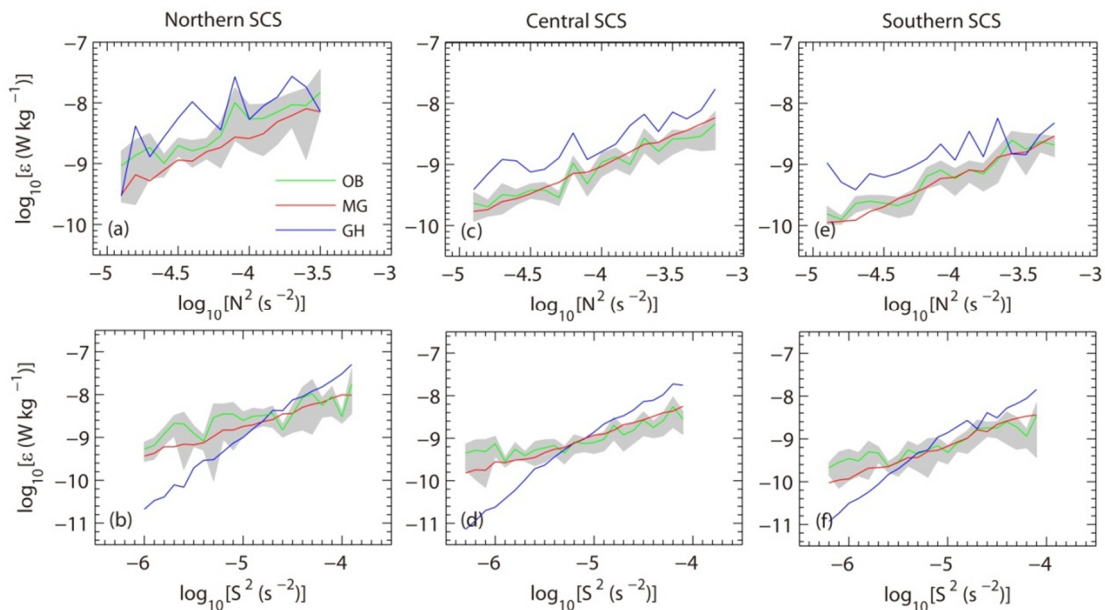
Fig. 8. Average dissipation rate calculated in bins of buoyancy frequency (N^2) and shear variance (S^2) for the northern SCS (a-b), central SCS (c-d), and southern SCS (e-f). The green, red, and blue curves are the results of the observation, MG

265   model, and GH model, respectively. The grey shading indicates the 95% bootstrapped confidence interval for the observed dissipation rates.

Comparing the three regions, we find that the confidence intervals of the observed dissipation rates in the northern SCS (Figs. 8a and 8b) were wider than those in the central and southern SCS (Figs. 8c-8f). In addition, the observed dissipation rates in the northern SCS were slightly larger and showed greater fluctuations than the MG model dissipation rates (Fig. 8a

270   and 8b). The wide confidence intervals and high observed dissipation rates in Figs. 8a and 8b mainly resulted from the elevated dissipation rates scattered in Fig. 7a. The MG model underestimated these elevated dissipation rates (comparing Fig.

7a with Fig. 7b). To explore this underestimation, we directly compared the model dissipation rates with the observed dissipation rates at three selected stations (Fig. 5, fourth column). For the stations from regions 3 and 4 (Figs. 5i and 5n), the relationships between the observed dissipation rates (pink curves) and the GH model dissipation rates (triangles) were poor,

275 with the GH model dissipation rates deviating from the observed data by one order of magnitude. Instead, the MG model dissipation rates (stars) fared better than the GH model dissipation rates against the observed data. For station 6 from region 1 (Fig. 5d), the MG model dissipation rates also agreed quite well with the observed data, except for the elevated dissipation rates induced by shear instability; for example, the MG model underestimated the elevated dissipation rates at depths of 175 to 195 m by more than one order of magnitude. The elevated dissipation rates scattered in Fig. 7a mainly resulted from the

280 dissipation rates induced by shear instability. However, the GH model dissipation rates seemed to agree with the elevated dissipation rates induced by shear instability (between 175 and 195 m). This agreement may be because the dissipation rates resulting from shear instability depends on the Richardson number and because the GH model also demonstrates Richardson number dependency.

4 Summary and discussion

285 We analyzed observations of turbulent dissipation and mixing in the SCS with microstructure data obtained from April 26 to May 23 2010. The observations are divided into four regions: region 1 in west of the Luzon Strait, region 2 in northeast of Hainan Island, region 3 in the central SCS, and region 4 in the southern SCS. In the vertical distribution, large ε values below the surface mixed layer were concentrated in the thermocline where the shear and stratification were strong. In the regional distribution, turbulent mixing was more active in west of the Luzon Strait with the mean $<\varepsilon>_T$ reaching 1.8×10^{-8} W

290 kg^{-1}, which is 9 times and 12 times larger than the values in the central (2.1×10^{-9} W kg^{-1}) and southern (1.5×10^{-9} W kg^{-1}) SCS, respectively. Elevated $<\kappa>_T$ were also found in west of the Luzon Strait, i.e., O (10^{-5} m^2 s^{-1}), which is an order of magnitude higher than the value of 5×10^{-6} m^2 s^{-1} in the open-ocean thermocline [Gregg, 1989]. This spatial pattern is consistent with the mixing distribution reported by Yang et al. [2016] who estimated the dissipation rate and diapycnal diffusivity with the Gregg-Henyey-Polzin parameterization and found strong turbulent mixing in west of the Luzon Strait. Our estimates of

295 diapycnal diffusivity in west of the Luzon Strait are similar to those of Tian et al. [2009] who estimated diapycnal diffusivity of O (10^{-5} m^2 s^{-1}) in the upper 500 m with fine-scale parameterization. In contrast, Yang et al. [2016] estimated the average diapycnal diffusivity in the upper 500 m as large as O (10^{-3} m^2 s^{-1}) in west of the Luzon Strait; the larger values may be attributed to various factors such as measuring methods and observation seasons.

The turbulent mixing in different regions displays different mixing features, to which shear variance and stratification have made significant contribution. In west of the Luzon Strait (region 1), the shear was stronger and the stratification was

300 weaker than those in other regions. Shear instability events occasionally occurred in this condition and produced elevated dissipation and diapycnal diffusivity. Although the turbulent patches induced by shear instability were occasional and sparse, they significantly contributed to the turbulent mixing in the water column. In the central and southern SCS (region 3 and

region 4), the water column was characterized by weak shear and strong stratification. Shear was no longer sufficient to
305   produce subcritical Richardson numbers and the turbulence was weak. The strong spatial correlation between high
dissipation rates and strong shear presented in the thermocline in west of the Luzon Strait suggests that shear was one of the
important drivers of the turbulent mixing. The strong shear may result from the internal tides or internal waves generated
near the Luzon Strait. Unfortunately, our observational data record was not long enough to identify these waves and analyze
their contribution to the mixing.

310   To predict realistic climate and circulation, mixing must be accurately represented in ocean models. Mapping of the
dissipation rates throughout the ocean is a daunting task. However, this task can be made considerably easier if mixing can
be estimated from more easily observed or modeled quantities, such as shear, stratification, and latitude. Two models (the
GH model and MG model) were evaluated for parameterizing the dissipation rate in the SCS. These two models were
derived from the eikonal model of Henyey et al., [1986] and are applicable to parameterize the dissipation controlled by
315   wave-wave interactions that transfer energy from large-scale waves to small-scale waves [MacKinnon and Gregg, 2005].
The GH model is based on the assumption that the waves are statistically stationary, with the energy of small-scale waves
and the shear of the large-scale waves maintain a particular relationship through the Garrett-Munk (GM) spectrum [Garrett
and Munk, 1975]. GH model is typically evaluated for the internal wave field with the GM spectral shape [Gregg, 1989].
The MG model is proposed by MacKinnon and Gregg [2003] to parameterize the turbulence over the continental shelf. It is
320   found to be suitable for the wave field in which the energy and shear are dominated by the near-inertial motions, internal
tides, or low frequency internal waves [MacKinnon and Gregg, 2003; Palmer et al., 2008; Xie et al., 2013].

       Statistical analysis shows the dissipation in the SCS to be proportional to both the shear and buoyancy frequencies, in
marked contrast to the predictions of the GH model, but consistent with the predictions of the MG model. The disagreement
of the GH model may be associated with the wave field in the SCS. Previous studies [Polzin et al., 1995; Wijesekera et al.,
325   1993] have indicated that the predictions of the GH model would exhibit departure from the observed dissipation by more
than one order of magnitude in regions where the wave field deviates from the GM spectrum. Thus, it is appropriate to
examine the wave flied in the SCS. Data obtained from six moorings deployed in the SCS (Fig. 1, yellow squares) were used
to estimate the horizontal kinetic energy spectra. Though the data were obtained from different periods, they reflected the
main characteristics of the wave field in the SCS. The spectra (Fig. 9) show significant peaks in the local inertial (f), diurnal
330   (O_1 and K_1), and semidiurnal (M_2) frequencies, which imply that energy was primarily dominated by the near-inertial
motions and internal tides. Within the internal wave band, significant peaks were also observed at higher tidal harmonic
frequencies such as D_3, D_4, and D_5. These energetic internal tides and harmonic internal waves cannot be well described by
the GM spectrum. Furthermore, the spectra deviated from the GM spectrum at high frequencies ($\sigma > 3$ cpd), which is
especially evident in the spectra of the moorings from west of the Luzon Strait (mooring 1) and the southern SCS (mooring
335   3). These observations are not supportive of the assumption that the GH model is based on. The GH model is typically
evaluated for the wave field with the GM spectral shape. In contrast, some of our observations support the MG model, that is
the wave field is dominated by near-inertial waves and internal tides and the dissipation rates scale positively with shear and

stratification. Overall, the MG model succeeds in parameterizing the turbulence in the SCS, except for some elevated dissipation rates induced by shear instability. The MG model tends to underestimate these elevated dissipation rates. This is

340   not surprising because the MG model, which is based on wave-wave interactions, represents bulk averages of turbulent properties and does not reproduce individual shear instability events [MacKinnon and Gregg, 2005].

The replication of the turbulence behavior greatly depends on the correct choice of model and appropriate tuning of the free parameters. The resolution of the shear and stratification is another factor in determining the success of models in parameterizing the turbulence [Palmer et al., 2013]. Although the MG model can reproduce the dissipation in the SCS for

345   our chosen vertical resolution (16 m), whether the distribution of the observed would change with finer resolution of shear and stratification is still an open problem. However, at least on the scale of internal waves (16 m), the MG model is clearly a better model than the GH model for the parameterization of turbulence in the upper ocean of the SCS, which provides a useful reference for modelers. Additional data with higher resolution are required to robustly fix this model in the near future.
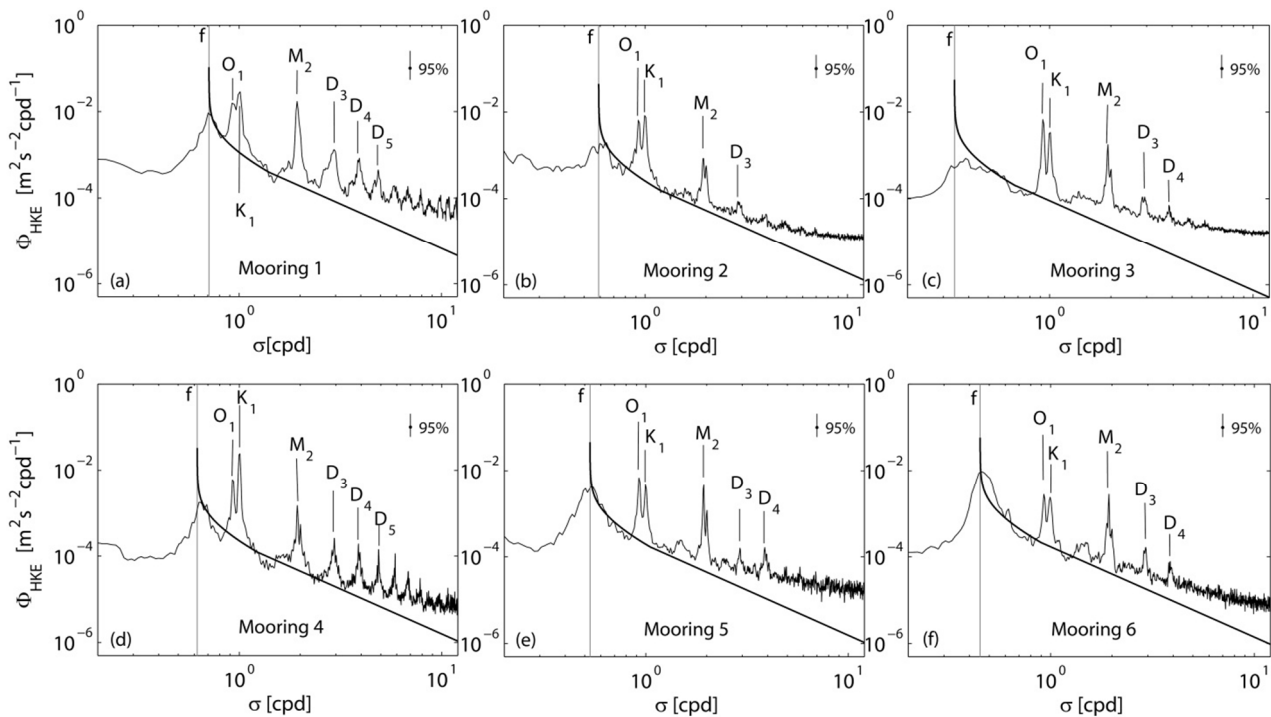
350   Fig. 9. (a-f) Rotary spectra (clockwise plus counterclockwise) of horizontal kinetic energy for the six moorings deployed in the SCS. Spectra are averaged over z ∈ [60:270] m. The canonical Garrett and Munk spectrum is shown for reference (smooth curve). The vertical lines represent various frequencies (f, O_1, K_1 …). The 95% statistical significance level is indicated by the vertical bar in the upper-right corner.

Author contribution

355   Xiao-Dong Shang and Gui-Ying Chen designed and carried out the experiments. Chang-Rong Liang prepared the manuscript with contributions from all co-authors.

Competing interests

The authors declare that they have no conflict of interest.

Acknowledgments

360   This work is supported by projects 2013CB430303, XDA11010202, 41376022, 41276021, and 41521005. The data were obtained from the South China Sea Institute of Oceanology.

References

Alford, M. H., et al.: The formation and fate of internal waves in the South China Sea, Nature, 521(7550), 65-69, doi:10.1038/nature14399, 2015.

365   Carter, G. S., and M. C. Gregg: Intense, variable mixing near the head of Monterey Submarine Canyon, J Phys Oceanogr, 32(11), 3145-3165, 2002.

Carter, G. S., M. C. Gregg, and M. A. Merrifield: Flow and mixing around a small seamount on Kaena Ridge, Hawaii, J Phys Oceanogr, 36(6), 1036-1052, doi:10.1175/Jpo2924.1, 2006.

Chang, M. H., R. C. Lien, T. Y. Tang, E. A. D'Asaro, and Y. J. Yang: Energy flux of nonlinear internal waves in northern

370   South China Sea, Geophys Res Lett, 33(3), doi:10.1029/2005 GL025196, 2006.

Egbert, G. D., and S. Y. Erofeeva: Efficient inverse modeling of barotropic ocean tides, J Atmos Ocean Tech, 19(2), 183-204.

Garrett, C., and W. Munk (1975), Space-Time Scales of Internal Waves - Progress Report, J Geophys Res, 80(3), 291-297, doi:10.1029/Jc080i003p00291, 2002.

Gregg, M. C.: Scaling Turbulent Dissipation in the Thermocline, J Geophys Res-Oceans, 94(C7), 9686-9698, doi:10.1029/

375   Jc094ic07p09686, 1989.

Henyey, F. S., J. Wright, and S. M. Flatte: Energy and Action Flow through the Internal Wave Field - an Eikonal Approach, J Geophys Res-Oceans, 91(C7), 8487-8495, doi:10.1029/ Jc091ic07p08487, 1986.

Klymak, J. M., J. N. Moum, J. D. Nash, E. Kunze, J. B. Girton, G. S. Carter, C. M. Lee, T. B. Sanford, and M. C. Gregg: An estimate of tidal energy lost to turbulence at the Hawaiian Ridge, J Phys Oceanogr, 36(6), 1148-1164, doi:10.1175/

380   Jpo2885.1, 2006.

Kunze, E., and J. M. Toole: Tidally driven vorticity, diurnal shear, and turbulence atop Fieberling Seamount, J Phys Oceanogr, 27(12), 2663-2693, doi:10.1175/1520-0485(1997)027, 1997.

Laurent, L. S.: Turbulent dissipation on the margins of the South China Sea, Geophys Res Lett, 35(23), doi:10.1029/2008gl035520, 2008.

385 Ledwell, J. R., E. T. Montgomery, K. L. Polzin, L. C. St Laurent, R. W. Schmitt, and J. M. Toole: Evidence for enhanced mixing over rough topography in the abyssal ocean, Nature, 403(6766), 179-182, doi:10.1038/35003164, 2000.

Ledwell, J. R., A. J. Watson, and C. S. Law: Evidence for Slow Mixing across the Pycnocline from an Open-Ocean Tracer-Release Experiment, Nature, 364(6439), 701-703, doi:10.1038/364701a0, 1993.

Lee, C. M., E. Kunze, T. B. Sanford, J. D. Nash, M. A. Merrifield, and P. E. Holloway: Internal tides and turbulence along 390 the 3000-m isobath of the Hawaiian Ridge, J Phys Oceanogr, 36(6), 1165-1183, doi: 10.1175/Jpo2886.1, 2006.

Lien, R. C., T. Y. Tang, M. H. Chang, and E. A. D'Asaro: Energy of nonlinear internal waves in the South China Sea, Geophys Res Lett, 32(5), doi:10.1029/2004GL022012, 2005.

Lozovatsky, I., Z. Liu, H. J. S. Fernando, J. Hu, and H. Wei: The TKE dissipation rate in the northern South China Sea, Ocean Dynam, 63(11-12), 1189-1201, 2013.

395 Lueck, R. G., and T. D. Mudge: Topographically induced mixing around a shallow seamount, Science, 276(5320), 1831-1833, doi:10.1126/science.276.5320.1831, 1997.

MacKinnon, J. A., and M. C. Gregg: Mixing on the late-summer New England shelf - Solibores, shear, and stratification, J Phys Oceanogr, 33(7), 1476-1492, doi:10.1175/1520-0485 (2003)033, 2003.

MacKinnon, J. A., and M. C. Gregg: Spring mixing: Turbulence and internal waves during restratification on the New 400 England shelf, J Phys Oceanogr, 35(12), 2425-2443, doi:10.1175/ Jpo2821.1, 2005.

Munk, W. H.: Abyssal recipes, paper presented at Deep Sea Research and Oceanographic Abstracts, Elsevier, 1966.

Nasmyth, P. W.: Oceanic turbulence, Retrospective Theses and Dissertations, 1919-2007, 1970.

Oakey, N. S.: Determination of the Rate of Dissipation of Turbulent Energy from Simultaneous Temperature and Velocity Shear Microstructure Measurements, J Phys Oceanogr, 12(3), 256-271, doi:10.1175/1520-0485(1982)012, 1982.

405 Osborn, T. R.: Estimates of the Local-Rate of Vertical Diffusion from Dissipation Measurements, J Phys Oceanogr, 10(1), 83-89, doi:10.1175/1520-0485(1980), 1980.

Palmer, M. R., J. A. Polton, M. E. Inall, T. P. Rippeth, J. A. M. Green, J. Sharples, and J. H. Simpson: Variable behavior in pycnocline mixing over shelf seas, Geophys Res Lett, 40(1), 161-166, doi:10.1029/2012gl054638, 2013.

Palmer, M. R., T. P. Rippeth, and J. H. Simpson: An investigation of internal mixing in a seasonally stratified shelf sea, J 410 Geophys Res-Oceans, 113(C12), doi: 10.1029/2007jc004531, 2008.

Polzin, K. L., J. M. Toole, and R. W. Schmitt: Finescale Parameterizations of Turbulent Dissipation, J Phys Oceanogr, 25(3), 306-328, doi:10.1175/1520-0485(1995), 1995.

Qu, T., H. Mitsudera, and T. Yamagata: Intrusion of the North Pacific waters into the South China Sea, J Geophys Res-Oceans, 105(C3), 6415-6424, doi:10.1029/1999jc900323, 2000.

415 Saenko, O. A., and W. J. Merryfield: On the effect of topographically enhanced mixing on the global ocean circulation, J Phys Oceanogr, 35(5), 826-834, doi:10.1175/Jpo2722.1, 2005.

Sandstrom, H., and J. A. Elliott: Internal Tide and Solitons on the Scotian Shelf - a Nutrient Pump at Work, J Geophys Res-Oceans, 89(Nc4), 6415-6426, doi:10.1029/Jc089ic04p06415, 1984.

Shaw, P. T.: The Seasonal-Variation of the Intrusion of the Philippine Sea-Water into the South China Sea, J Geophys Res-
420 Oceans, 96(C1), 821-827, doi:10.1029/90jc02367, 1991.

Tian, J. W., Q. X. Yang, and W. Zhao: Enhanced Diapycnal Mixing in the South China Sea, J Phys Oceanogr, 39(12), 3191-3203, doi: 10.1175/2009jpo3899.1, 2009.

van der Lee, E. M., and L. Umlauf: Internal wave mixing in the Baltic Sea: Near-inertial waves in the absence of tides, J Geophys Res-Oceans, 116(C10), doi: 10.1029/2011jc007072, 2011.

425 Wijesekera, H., L. Padman, T. Dillon, M. Levine, C. Paulson, and R. Pinkel: The Application of Internal-Wave Dissipation Models to a Region of Strong Mixing, J Phys Oceanogr, 23(2), 269-286, 1993.

Wolk, F., H. Yamazaki, L. Seuront, and R. G. Lueck: A new free-fall profiler for measuring biophysical microstructure, J Atmos Ocean Tech, 19(5), 780-793, doi:10.1175/1520-0426 (2002)019, 2002.

Wu, and Y. C. Hsin: The forcing mechanism leading to the Kuroshio intrusion into the South China Sea, J Geophys Res-
430 Oceans, 117(C7), doi:10.1029/2012jc007968, 2012.

Wu, Z. Jing, S. Riser, and M. Visbeck: Seasonal and spatial variations of Southern Ocean diapycnal mixing from Argo profiling floats, Nat Geosci, 4(6), 363-366, doi:10.1038/Ngeo1156, 2011.

Xie, X. H., Y. Cuypers, P. Bouruet-Aubertot, B. Ferron, A. Pichon, A. Lourenco, and N. Cortes: Large-amplitude internal tides, solitary waves, and turbulence in the central Bay of Biscay, Geophys Res Lett, 40(11), 2748-2754,
435 doi:10.1002/Grl.50533, 2013.

Yang, Q. X., J. W. Tian, W. Zhao, X. F. Liang, and L. Zhou: Observations of turbulence on the shelf and slope of northern South China Sea, Deep-Sea Res Pt I, 87, 43-52, doi:10.1016/j.dsr. 2014.02.006, 2014.

Yang, Q. X., W. Zhao, X. Liang, and J. Tian: Three-Dimensional Distribution of Turbulent Mixing in the South China Sea, J Phys Oceanogr, 46(3), 769-788, doi:10.1175/JPO-D-14-0220.1, 2016.

440